Role of Sn^{2+} in the Band Structure of SnM_2O_6 and $Sn_2M_2O_7$ (M = Nb and Ta) and Their Photocatalytic Properties

Yasuhiro Hosogi,[†] Yoshiki Shimodaira,[†] Hideki Kato,[†] Hisayoshi Kobayashi,[‡] and Akihiko Kudo*[,†,§]

Department of Applied Chemistry, Faculty of Science, Tokyo University of Science, 1-3 Kagurazaka, Shinjyuku-Ku, Tokyo 162-0825, Japan, Department of Chemistry and Materials Technology, Kyoto Institute of Technology, Matsugasaki, Sakyo-ku, Kyoto 606-8585, Japan, and Core Research for Evolutional Science and Technology, Japan Science and Technology Agency (CREST, JST), 4-1-8 Honcho, Kawaguchi-shi, Saitama 332-0012, Japan

Received June 14, 2007. Revised Manuscript Received October 22, 2007

The photocatalytic properties of metal oxides consisting of Sn^{2+} with a $5s^2$ configuration were studied to find new visible light responsive photocatalysts. The band gaps of $Ca_2Ta_2O_7$, $Sn_2Ta_2O_7$, and $Sn_2Nb_2O_7$ were found to be 4.8, 3.0, and 2.3 eV, respectively. Density functional calculations revealed that the valence band levels formed with Sn 5s orbitals were more negative than those with O 2p orbitals. The result is that niobates and tantalates containing Sn^{2+} have narrow band gaps compared with typical niobates and tantalates. $SnNb_2O_6$ showed photocatalytic activity for H_2 and O_2 evolution from aqueous solutions containing sacrificial reagents (methanol and Ag^+) under visible light irradiation ($\lambda > 420$ nm). Moreover, the photocatalytic activity of $SnNb_2O_6$ depended on the material used as the Sn source. $SnNb_2O_6$ synthesized from $Sn_3O_2(OH)_2$ showed higher activity for H_2 and O_2 evolution than that synthesized from commercial SnO, which included a small amount of SnO_2. $SnNb_2O_6$ synthesized from $Sn_3O_2(OH)_2$ showed activity for O_2 evolution under visible light, even without IrO_2 as a cocatalyst, whereas that synthesized from commercial SnO showed activity under irradiation only when an IrO_2 cocatalyst was loaded. The activity of $SnNb_2O_6$ synthesized from SnO was improved by IrO_2 cocatalyst loading.

1. Introduction

Photocatalytic water splitting has been studied intensively as one of the possible solutions to the energy problem. It has been reported that many metal oxide[1–4] and Ge_3N_4[5] photocatalysts can split water into H_2 and O_2 in stoichiometric amounts with high efficiencies under ultraviolet light irradiation. Recently, Domen and co-workers have reported water splitting over a GaN−ZnO photocatalyst under visible light irradiation.[6] Many visible-light-driven photocatalysts that show activity for H_2 or O_2 evolution from aqueous solutions containing a sacrificial reagent have also been found. WO_3,[7] $RbPb_2Nb_3O_{10}$,[8] $BiVO_4$,[9] $AgNbO_3$,[10] TiO_2:Cr,Sb,[11] Ag_3VO_4[12] TiO_2:Ni,Ta,[13] and TiO_2:Rh,Sb[14] have been reported to be active metal oxide photocatalysts for O_2 evolution. $HPb_2Nb_3O_{10}$,[8] $SrTiO_3$:Cr,Sb,[11] $SrTiO_3$:Cr,Ta,[15] $SrTiO_3$:Rh,[16] and $SrTiO_3$:Ni[13] are metal oxide photocatalysts that can reduce water to form H_2 under visible light irradiation in the presence of sacrificial reagents. Non-oxide photocatalysts have also been developed. Metal (oxy)nitrides and oxysulfides such as TaON,[17] Ta_3N_5,[17] $LaTiO_2N$,[18] $TiN_xO_yF_z$,[19] and $Sm_2Ti_2S_2O_5$[20] have potential for H_2 and O_2 evolution under visible light irradiation from aqueous solutions containing sacrificial reagents, even though they are not active for overall water splitting.

In photosynthesis by green plants, carbohydrates and O_2 are formed from CO_2 and H_2O using the so-called Z-scheme

* Corresponding author: e-mail a-kudo@rs.kagu.tus.ac.jp; Fax +81-35261-4631.
[†] Tokyo University of Science.
[‡] Kyoto Institute of Technology.
[§] Japan Science and Technology Agency.

(1) Domen, K.; Kondo, J. N.; Hara, M.; Takata, T. *Bull. Chem. Soc. Jpn.* **2000**, *73*, 1307.
(2) Kudo, A.; Kato, H.; Tsuji, I. *Chem. Lett.* **2004**, *33*, 1534.
(3) Sato, J.; Kobayashi, H.; Ikarashi, K.; Saito, N.; Nishiyama, H.; Inoue, Y. *J. Phys. Chem. B* **2004**, *108*, 4369.
(4) Kato, H.; Asakura, K.; Kudo, A. *J. Am. Chem. Soc.* **2003**, *125*, 3082.
(5) Sato, J.; Saito, N.; Yamada, Y.; Maeda, K.; Takata, T.; Kondo, J. N.; Hara, M.; Kobayashi, H.; Domen, K.; Inoue, Y. *J. Am. Chem. Soc.* **2005**, *127*, 4150.
(6) Maeda, K.; Teramura, K.; Lu, D.; Takata, T.; Saito, N.; Inoue, Y.; Domen, K. *Nature (London)* **2006**, *440*, 295.
(7) Darwent, J. R.; Mills, A. *J. Chem. Soc., Faraday Trans. 2* **1982**, *78*, 359.
(8) Yoshimura, J.; Ebina, Y.; Tanaka, A.; Kondo, J.; Domen, K. *J. Phys. Chem.* **1993**, *97*, 1970.
(9) Kudo, A.; Omori, K.; Kato, H. *J. Am. Chem. Soc.* **1999**, *121*, 11459.
(10) Kato, H.; Kobayashi, H.; Kudo, A. *J. Phys. Chem. B* **2002**, *106*, 12441.
(11) Kato, H.; Kudo, A. *J. Phys. Chem. B* **2002**, *106*, 5029.
(12) Konta, R.; Kato, H.; Kobayashi, H.; Kudo, A. *Phys. Chem. Chem. Phys.* **2003**, *5*, 3061.
(13) Niishiro, R.; Kato, H.; Kudo, A. *Phys. Chem. Chem. Phys.* **2005**, *7*, 2241.
(14) Niishiro, R.; Konta, R.; Kato, H.; Chun, W. J.; Asakura, K.; Kudo, A. *J. Phys. Chem. C*, in press.
(15) Ishii, T.; Kato, H.; Kudo, A. *J. Photochem. Photobiol. A* **2004**, *163*, 181.
(16) Konta, R.; Ishii, T.; Kato, H.; Kudo, A. *J. Phys. Chem. B* **2004**, *108*, 8992.
(17) Hara, M.; Hitoki, G.; Takata, T.; Kondo, J. N.; Kobayashi, H.; Domen, K. *Stud. Surf. Sci. Catal.* **2003**, *145*, 169.
(18) Kasahara, A.; Nukumizu, K.; Hitoki, G.; Takata, T.; Kondo, J. N.; Hara, M.; Kobayashi, H.; Domen, K. *J. Phys. Chem. A* **2002**, *106*, 6750.
(19) Nukumizu, K.; Nunoshige, J.; Takata, T.; Kondo, J. N.; Hara, M.; Kobayashi, H.; Domen, K. *Chem. Lett.* **2003**, *32*, 196.
(20) Ishikawa, A.; Takata, T.; Kondo, J. N.; Hara, M.; Kobayashi, H.; Domen, K. *J. Am. Chem. Soc.* **2002**, *124*, 13547.

10.1021/cm071588c CCC: $40.75
Published on Web 01/01/2008

reaction, which is composed of two photoexcitation processes. A photocatalytic system that involves two photoexcitation processes, with separate photocatalysts for H_2 and O_2 evolution, and an intermediary electron relay, is called a Z-scheme because of the similarity to the natural photosynthesis of green plants. Recently, overall water splitting under visible light irradiation has been achieved using Z-scheme systems.[21–25] These successful results for the construction of Z-scheme systems strongly motivate the development of visible-light-driven photocatalysts, even if they are active for only one of the half-reactions of water splitting, i.e., H_2 or O_2 evolution.

Metal oxide compounds containing lead, such as $Pb_2Nb_2O_7$, are good ferroelectric materials. The properties of Pb^{2+} materials arise due to the presence of the Pb^{2+} lone-pair electrons. However, the use of lead leads to environmental problems. Therefore, metal oxides containing Sn^{2+}, which also has lone-pair electrons, instead of Pb^{2+}, have been studied as Pb-free materials. The syntheses of $SnNb_2O_6$, with the foordite structure, $SnTa_2O_6$, with the thoreaulite structure, and $Sn_2M_2O_7$, with the pyrochlore structure (M = Nb and Ta), have been reported.[26–29] However, their photocatalytic properties have thus far not been investigated.

The visible light response of the $BiVO_4$ photocatalyst for O_2 evolution is due to its valence band, which consists of Bi^{3+} with a $6s^2$ electron configuration. Therefore, the present authors have also paid attention to Sn^{2+}, which has a $5s^2$ electron configuration. In a previous paper, we reported that $SnNb_2O_6$ was an active photocatalyst for H_2 evolution from an aqueous methanol solution under visible light irradiation, and the valence band of $SnNb_2O_6$ was formed from Sn 5s and O 2p orbitals, resulting in a decrease in the band gap.[30] However, the $SnNb_2O_6$ photocatalyst did not show activity for O_2 evolution. Moreover, the band structures of other niobates and tantalates containing Sn^{2+} ($Sn_2Nb_2O_7$, $Sn_2Ta_2O_7$, and $SnTa_2O_6$) have not been clarified. In the present study, the band structures of $Sn_2Nb_2O_7$, $Sn_2Ta_2O_7$, $SnNb_2O_6$, and $SnTa_2O_6$ were systematically investigated, by diffuse reflectance spectra and plane-wave-based density functional calculations, to clarify the role of Sn^{2+} in the valence band. Moreover, the preparation methods for $SnNb_2O_6$ and the effect of a colloidal IrO_2 cocatalyst on O_2 evolution were studied in order to improve the photocatalytic activity.

2. Experimental Section

Niobates and tantalates containing Sn^{2+} were prepared by solid-state reaction in flowing nitrogen. Starting materials used were as follows: SnO (Wako Pure Chemical; purity, 99.9%), Nb_2O_5 (Kanto Chemical; purity, 99.95%), and Ta_2O_5 (Rare Metallic; purity, 99.99%). $Sn_3O_2(OH)_2$ was prepared by hydrolysis of $SnCl_2$ (Wako; purity, 99.9%) with NH_3(aq). $Sn_3O_2(OH)_2$ was calcined at 373 K for 1 h in air if necessary. Mixtures of the starting materials, SnO or $Sn_3O_2(OH)_2$, and Nb_2O_5 or Ta_2O_5, were calcined at 973–1273 K for 6–40 h in flowing nitrogen using an alumina boat. The crystal structures of the synthesized metal oxides were confirmed by powder X-ray diffraction (Rigaku, MiniFlex) with use of the JCPDS database.[31] Cocatalysts for H_2 or O_2 evolution were loaded if necessary. Pt cocatalysts for H_2 evolution were loaded in situ by a photodeposition method using H_2PtCl_6. The preparation and loading of colloidal IrO_2 cocatalyst were carried out according to the report of Hara et al.[20] The colloidal IrO_2 cocatalysts were loaded on the photocatalysts by adsorption.

Diffuse reflectance spectra were measured using a UV–vis–NIR spectrometer with an integrating sphere (JASCO, U-best570) and were converted from reflection to absorbance by the Kubelka–Munk method. The amount of Sn^{2+} in bulk $SnNb_2O_6$ was estimated from the weight gain after calcination in air using thermogravimetric analysis (TGA, ULVAC, TGD-9600). The oxidation states of Sn on the surfaces of the materials were investigated by X-ray photoelectron spectroscopy (XPS, KRATOS, ESCA-3400). The binding energies of each spectrum were corrected by reference to the C 1s peak (284.2 eV). The catalyst morphologies were observed using a scanning electron microscope (SEM, JEOL, JSM-6700F).

The plane-wave-based density functional theory (PW-DFT) calculations were carried out for $SnNb_2O_6$ of the foordite type, $SnTa_2O_6$ of the thoreaulite type, and $Ca_2Ta_2O_7$ and $Sn_2Ta_2O_7$ of the pyroclore type by employing the CASTEP program[32] and initial crystal parameters indicated in the ICSD (Inorganic Crystal Structure Database).[33–36] The ICSD crystal parameters were optimized by the BFGS (Broyden–Fletcher–Goldfarb–Shanno) method using a starting Hessian that was recursively updated during geometry optimization.[37] The initial and optimized crystal parameters are shown in the Supporting Information (Tables S1–S8). The symmetry treatment of the atom positions by space group was ensured during the geometry optimization, although lattice parameters were imposed general linear constraints on unit cell. The core electrons were replaced with ultrasoft core potentials,[38] and the valence electronic configurations for Sn, Ca, Ta, Nb, and O atoms were $5s^25p^2$, $3s^23p^64s^2$, $6s^25d^3$, $4s^24p^65s^14d^4$, and $2s^22p^4$, respectively. The PW-DFT calculations were carried out using primitive unit cells of $[SnNb_2O_6]_2$, $[SnTa_2O_6]_2$, $[Sn_2Ta_2O_7]_8$, and $[Ca_2Ta_2O_7]_8$. The total numbers of electrons were 132, 100, 448, and 576, and the numbers of occupied molecular orbitals were 66, 50, 224, and 288, respectively. The kinetic energy cutoffs were taken to be 300 eV. The type of DFT exchange-correlation potential used in the

(21) Sayama, K.; Mukasa, K.; Abe, R.; Abe, Y.; Arakawa, H. *J. Photochem. Photobiol. A* **2002**, *148*, 71.
(22) Kato, H.; Hori, M.; Konta, R.; Shimodaira, Y.; Kudo, A. *Chem. Lett.* **2004**, *33*, 1348.
(23) Abe, R.; Takata, T.; Sugihara, H.; Domen, K. *Chem. Commun.* **2005**, 3829.
(24) Abe, R.; Sayama, K.; Sugihara, H. *J. Phys. Chem. B* **2005**, *109*, 16052.
(25) Kato, H.; Iwase, A.; Sasaki, Y.; Kudo, A. *Bull. Chem. Soc. Jpn.*, in press.
(26) Bodiot, D. *Rev. Chim. Miner.* **1968**, *5*, 569.
(27) Brisse, F.; Stewart, D. J.; Seidl, V.; Knop, O. *Can. J. Chem.* **1972**, *50*, 3648.
(28) Cruz, L. P.; Savariault, J. M.; Rocha, J.; Jumas, J. C.; Pedrosa, de jesus J. D. *J. Solid State Chem.* **2001**, *156*, 349.
(29) Cerny, P.; Fransolet, A.-M.; Ercit, T. S.; Chapman, R. *Can. Mineral.* **1988**, *26*, 889.
(30) Hosogi, Y.; Tanabe, K.; Kato, H.; Kobayashi, H.; Kudo, A. *Chem. Lett.* **2004**, *33*, 28.
(31) JCPDS Cards ($SnTa_2O_6$: 23-0597; $SnNb_2O_6$: 84-1810; $Sn_2Ta_2O_7$: 74-1353; and $Sn_2Nb_2O_7$: 23-0593).
(32) Payne, M. C.; Teter, M. P.; Allan, D. C.; Arias, T. A.; Joannopoulos, J. D. *Rev. Mod. Phys.* **1992**, *64*, 1045.
(33) Inorganic Crystal Structure Database ($SnNb_2O_6$: #202827; $SnTa_2O_6$: # 54078; $Ca_2Ta_2O_7$: #27121; $Sn_2Ta_2O_7$: #27119).
(34) Ercit, T. S.; Cerny, P. *Can. Mineral.* **1988**, *26*, 899.
(35) Maksimova, N. V.; Ilyukhin, V. V.; Belov, N. V. *Dokl. Akad. Nauk SSSR* **1975**, *223*, 1115.
(36) Gasperin, M. C. R. *Hebd. Seances Acad. Sci.* **1955**, *240*, 2340.
(37) Pfrommer, B. G.; Cote, M.; Louie, S. G.; Cohen, M. L. *J. Comput. Phys.* **1997**, *131*, 133.
(38) Vanderbilt, D. *Phys. Rev.* **1990**, *B41*, 7892.

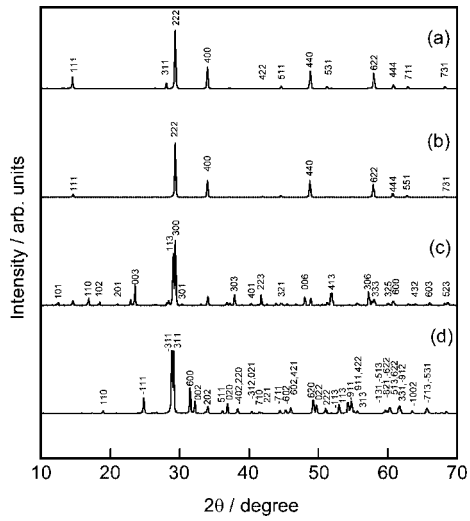

Figure 1. XRD patterns of (a) $Sn_2Ta_2O_7$, (b) $Sn_2Nb_2O_7$, (c) $SnTa_2O_6$, and (d) $SnNb_2O_6$.

calculations was chosen a gradient-corrected (GGA) function[39] and a PBE (Perdew, Bruke, and Enzerhof) function method.[40]

The photocatalytic reactions, H_2 evolution from an aqueous methanol solution (10 vol %) and O_2 evolution from an aqueous silver nitrate solution (0.05 M), were conducted in a gas-tight circulation system. Photocatalyst powder (0.3 g) was dispersed in the solution (150 mL) by a magnetic stirrer in a cell with a top window made of Pyrex glass. The light source was a 300 W Xe illuminator (Perkin-Elmer; CERMAX PE-300BF) equipped with cutoff filters (Kenko). The amounts of H_2 and O_2 evolved were determined using gas chromatography (Shimadzu GC-8A; TCD, Ar carrier gas).

3. Results and Discussion

3.1. Syntheses and Band Structures of SnM_2O_6 and $Sn_2M_2O_7$ (M = Nb and Ta). Figure 1 shows the XRD patterns of the Sn^{2+}-containing niobate and tantalate powders prepared by solid-state reaction. These prepared materials were confirmed to possess single phases of $SnNb_2O_6$, $Sn_2Nb_2O_7$, and $Sn_2Ta_2O_7$. The crystal structures of $Sn_2Nb_2O_7$ and $Sn_2Ta_2O_7$ were of the pyrochlore type, while that of $SnNb_2O_6$ was of the foordite type. It has been reported that $SnTa_2O_6$ has two crystal structures (JCPDS: 23-597, 87-358).[26,34] The $SnTa_2O_6$ prepared in the present study exhibited a crystal structure that agreed with the data shown in JCPDS: 23-597, although small amounts of impurities such as $Sn_2Ta_2O_7$ and Ta_2O_5 were present.

Figure 2 shows diffuse reflectance spectra for $Sn_2Nb_2O_7$, $Sn_2Ta_2O_7$, $SnNb_2O_6$, and $SnTa_2O_6$. The absorption edges were steep, indicating that they were due to band gap transitions, from valence band to conduction band. The band gap for $Sn_2Ta_2O_7$ was estimated to be 3.0 eV. In contrast, it has been reported that the band gap for $Ca_2Ta_2O_7$, with the pyrochlore structure, was 4.4 eV.[41] This result suggested that Sn^{2+} contributed to the band gap narrowing. Furthermore, the band gap of $Sn_2Nb_2O_7$, with the pyrochlore structure,

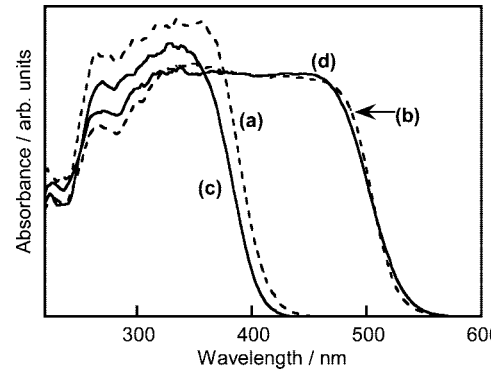

Figure 2. Diffuse reflectance spectra of (a) $Sn_2Ta_2O_7$, (b) $Sn_2Nb_2O_7$, (c) $SnTa_2O_6$, and (d) $SnNb_2O_6$.

was 2.3 eV, which was narrower than that of $Sn_2Ta_2O_7$. The narrowing of the band gap of $Sn_2Nb_2O_7$ was due to the conduction band level, consisting of an Nb 4d orbital, which was more positive than that of the Ta 5d orbital. There were small differences in diffuse reflectance spectra between SnM_2O_6 and $Sn_2M_2O_7$ (M = Nb or Ta).

We calculated the band structures of $Sn_2Ta_2O_7$ and $Ca_2Ta_2O_7$ by the PW-DFT method in order to clarify the effect of Sn^{2+} on the valence band. Figure 3 shows the band structures and the densities of states (DOS) for $Sn_2Ta_2O_7$ and $Ca_2Ta_2O_7$. The DOS was divided into the angular momentum of atomic orbitals (AOs), represented by different line colors. In an effort to obtain more exact information on the atom-specific character of each band, the DOS was further decomposed into the AO-projected DOS (PDOS) in terms of atomic and angular momentum contributions. Figure 4 shows the AO-PDOS for Sn, Ca, Ta, and O atoms in the lower energy region (−10 to 0 eV) of the occupied bands and the higher energy region (0 to 9 eV) of unoccupied bands. The occupied bands of $Ca_2Ta_2O_7$ were composed of three bands, consisting of Ca 3p, O 2s, and O 2p orbitals, from the low-energy side. The occupied bands, containing the top of the valence band (HOMO) on the high-energy side, consisted of O 2p orbitals (#121–288), as shown in Figures 3a and 4a. On the other hand, the conduction band, including the LUMO, consisted of Ta 5d orbitals (#289–336).

The occupied bands of $Sn_2Ta_2O_7$ were composed of O 2s, Sn 5s, O 2p, and Sn 5s (+O 2p) orbitals from the low-energy side, as shown in Figure 3b. The valence band was composed of three parts. The lowest part was the occupied band, consisting of the Sn 5s orbitals (#57–200). The middle part was the band consisting of O 2p orbitals (#201–224). Sn 5s orbitals (#225–240) were observed again at the highest part, containing the top of the valence band (HOMO). This was also confirmed from Figure 4b. The conduction band, including the LUMO, consisted of Ta 5d orbitals (#241–290), also as for $Ca_2Ta_2O_7$.

The energy levels of the band structure and DOS obtained by the PW-DFT calculations do not indicate the absolute values because the top end of the occupied orbitals is set to be zero. However, we can compare the degree of dispersion of the bands of $Ca_2Ta_2O_7$ and $Sn_2Ta_2O_7$ because the same Bloch function and space group were used. The valence bandwidth of $Ca_2Ta_2O_7$ was ca. 7.3 eV. In contrast, that of $Sn_2Ta_2O_7$ was ca. 8.5 eV, which was wider than that of

(39) White, J. A.; Bird, D. M. *Phys. Rev. B* **1994**, *50*, 4954.
(40) Perdew, J. P.; Bruke, K.; Ernzerhof, M. *Phys. Rev. Lett.* **1996**, *77*, 3865.
(41) Ikeda, S.; Fubuki, M.; Takahara, Y. K.; Matsumura, M. *Appl. Catal., A* **2006**, *300*, 186.

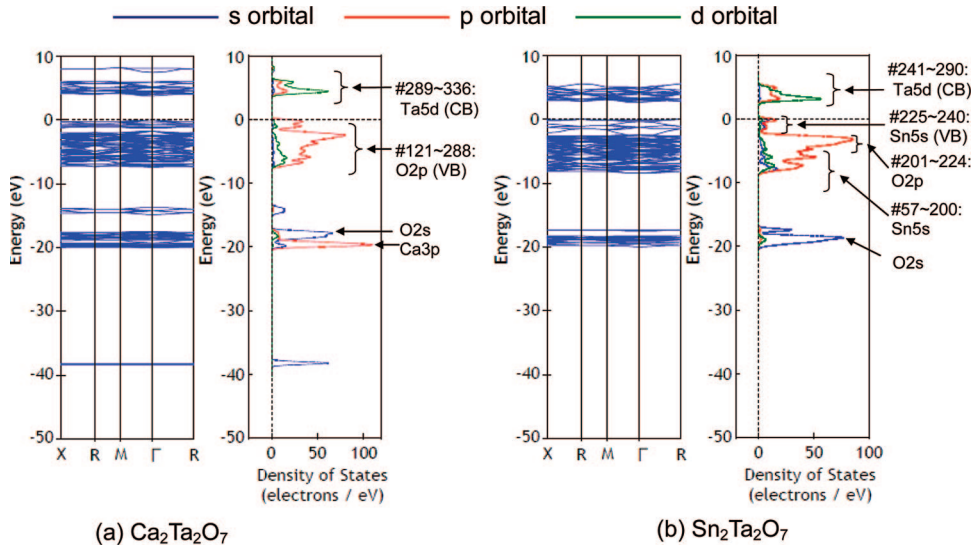

Figure 3. Electronic band structures and densities of states of (a) $Ca_2Ta_2O_7$ and (b) $Sn_2Ta_2O_7$ calculated by a density functional method.

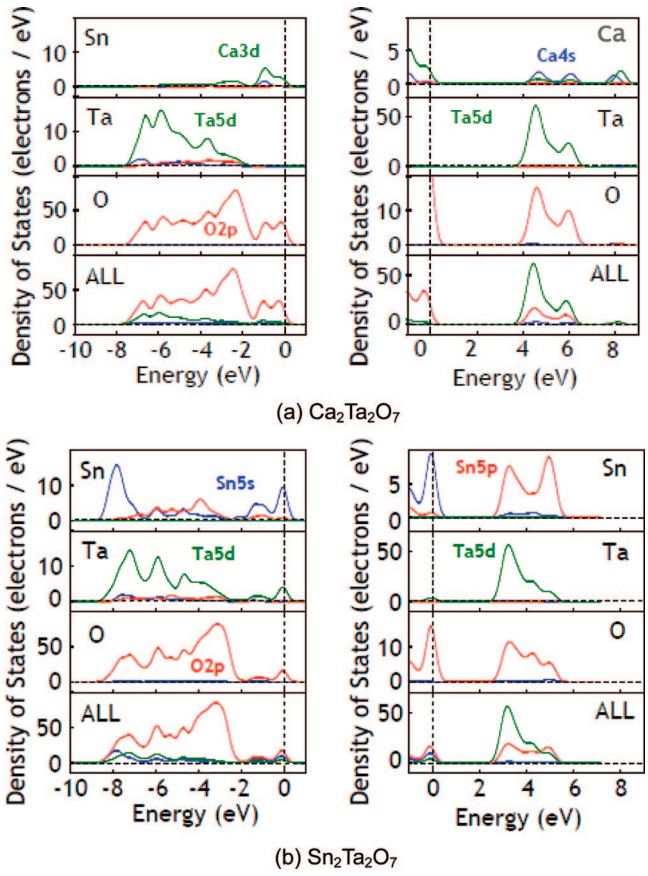

Figure 4. Partial densities of states of (a) $Ca_2Ta_2O_7$ and (b) $Sn_2Ta_2O_7$.

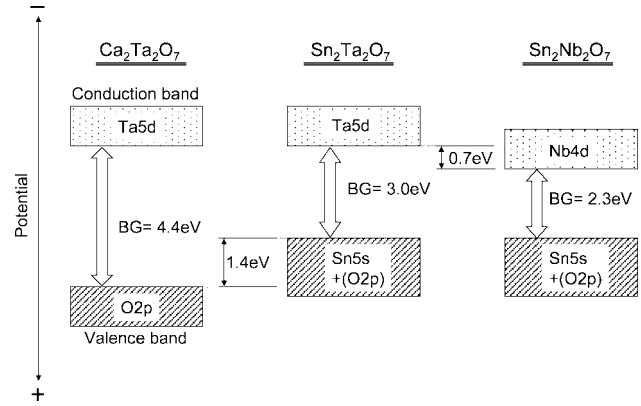

Figure 5. Band structures of $Ca_2Ta_2O_7$ and $Sn_2M_2O_7$ (M = Ta, Nb).

$Ca_2Ta_2O_7$ because the Sn 5s orbitals contributed to the valence band formation. Consequently, these calculation results suggested that the mobility of photogenerated holes in the valence band of $Sn_2Ta_2O_7$ was higher than that of $Ca_2Ta_2O_7$. The calculated band gaps of $Sn_2Ta_2O_7$ and $Ca_2Ta_2O_7$ were 2.66 and 3.78 eV, respectively. Although band gaps calculated by the present method are usually narrower than the actual ones, the order of the calculated band gaps was the same as that experimentally determined from diffuse reflectance spectra. The calculation for $Sn_2Nb_2O_7$ was unable to be carried out because the crystal parameters have not been reported.

Figure 5 shows the band structures of $Ca_2Ta_2O_7$, $Sn_2Ta_2O_7$, and $Sn_2Nb_2O_7$ derived from diffuse reflectance spectra and PW-DFT calculations. The potential of the conduction band minimum of $Ca_2Ta_2O_7$ should be similar to that of $Sn_2Ta_2O_7$ because they have the same pyrochlore structure and conduction band consisting of Ta 5d orbitals. Consequently, the band gap of $Sn_2Ta_2O_7$ was 1.4 eV narrower than that of $Ca_2Ta_2O_7$ because the Sn 5s orbitals formed new valence bands at a more negative level than the O 2p orbitals. The differences (1.4 eV) in the band gap and the HOMO level between $Ca_2Ta_2O_7$ and $Sn_2Ta_2O_7$ were reasonable, judging from the difference (1.2 eV) in the valence bandwidth, as mentioned above. On the other hand, the band gap of $Sn_2Nb_2O_7$ was 0.7 eV narrower than that of $Sn_2Ta_2O_7$. The difference in the band gap between $Sn_2Nb_2O_7$ and $Sn_2Ta_2O_7$ was almost the same as that between $Sr_2Nb_2O_7$ and $Sr_2Ta_2O_7$.[42] Therefore, it was considered that the valence band of $Sn_2Nb_2O_7$ was formed from Sn 5s orbitals, and the potential was similar to that of $Sn_2Ta_2O_7$. The band gap of $Sn_2Nb_2O_7$ was narrower

(42) Kudo, A.; Kato, H.; Nakagawa, S. *J. Phys. Chem. B* **2000**, *104*, 571.

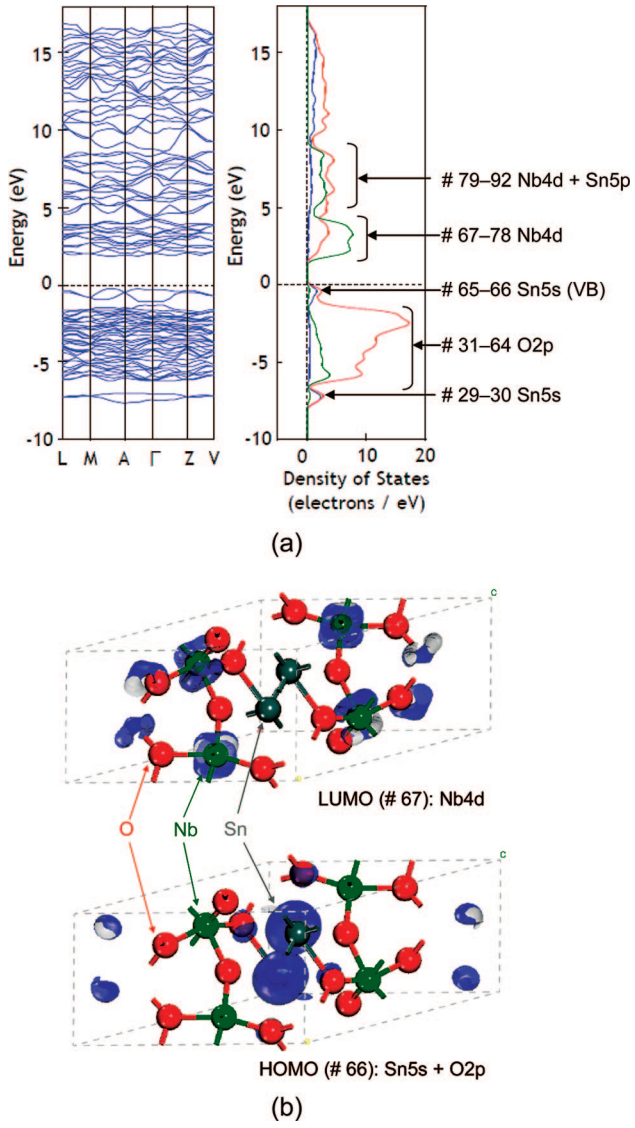

Figure 6. (a) Electronic band structures, densities of states, and (b) density contour maps for the LUMO and HOMO of $SnNb_2O_6$.

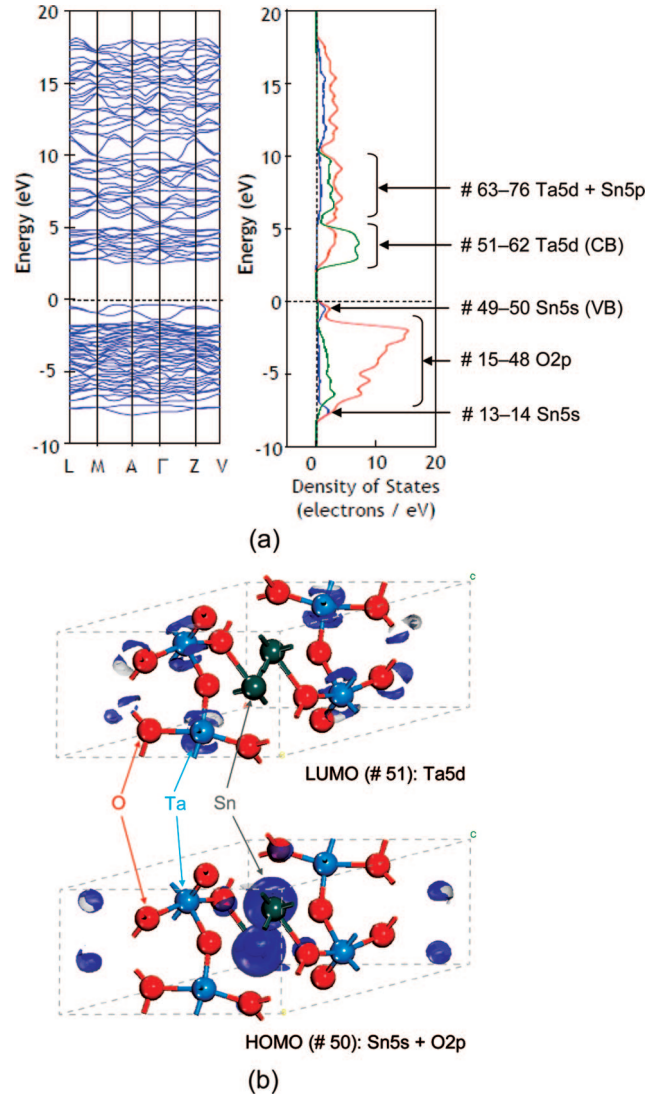

Figure 7. (a) Electronic band structures, densities of states, and (b) density contour maps for the LUMO and HOMO of $SnTa_2O_6$.

than that of $Sn_2Ta_2O_7$ because the Nb 4d orbitals formed a conduction band at a more positive level than the Ta 5d orbitals.

Figure 6a shows the band structures and the densities of states of $SnNb_2O_6$, which is active under visible light irradiation.[30] The density contour maps for the LUMOs and HOMOs of $SnNb_2O_6$ are shown in Figure 6b. The valence band of $SnNb_2O_6$ was composed of three parts, as was that of $Sn_2Ta_2O_7$. The lowest part was the occupied bands, consisting of Sn 5s orbitals (#29 and 30). The middle part was a band consisting of O 2p orbitals (#31–64). Moreover, the highest part, containing the top of the valence band (HOMO), mainly consisted of Sn 5s orbitals (#65 and 66). This was also confirmed from Figure 6b. The conduction bands, including the LUMO, consisted of Nb 4d orbitals (#67–78). The crystal parameters for the $SnTa_2O_6$, obtained in the present study, have not been reported. Thus, we calculated the band structures and the densities of states of the thoreaulite-type $SnTa_2O_6$, as shown in Figure 7. These were very similar to those of $SnNb_2O_6$. The overlaps of the Sn 5s and O 2p orbitals in

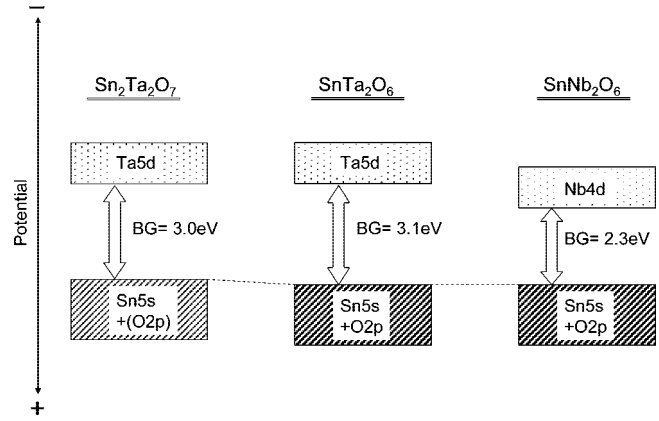

Figure 8. Band structures of SnM_2O_6 (M = Ta, Nb).

the valence band maxima of $SnNb_2O_6$ and $SnTa_2O_6$ were larger than that of $Sn_2Ta_2O_7$. Consequently, the mobility of the photogenerated holes in the valence bands of $SnNb_2O_6$ and $SnTa_2O_6$ was higher than that of $Sn_2Ta_2O_7$. The calculated band gaps of $SnNb_2O_6$ and $SnTa_2O_6$ were 2.10 and 2.81 eV, respectively. Figure 8 shows the band structures of SnM_2O_6 (M = Ta, Nb) derived from diffuse

reflectance spectra and PW-DFT calculations. The valence band of $SnNb_2O_6$ was formed from Sn 5s orbitals, as was as that of $Sn_2M_2O_7$ (M = Nb, Ta), resulting in the band gap narrowing. However, the levels of the conduction and valence bands of $SnNb_2O_6$ might be different from those of $Sn_2Nb_2O_7$ because the crystal structure and the Sn:Nb ratio are different from each other. The valence band level of $SnNb_2O_6$ should shift to a more positive value than that of $Sn_2M_2O_7$ (M = Nb, Ta) because the valence bands were controlled by the degree of contribution of the Sn 5s orbitals.

It was clarified that the band gap narrowing of metal oxides containing Sn^{2+} was due to the contribution of Sn 5s orbitals to the valence band formation. The band gaps were 1.0–1.8 eV smaller than those of other tantalates, e.g., $SrTa_2O_6$ and $Sr_2Ta_2O_7$. The band gaps of $SnNb_2O_6$ and $Sn_2Nb_2O_7$ (2.3 eV) were quite narrow among niobate photocatalysts such as $Sr_2Nb_2O_7$.[42] The effect of the Sn 5s orbitals on the negative shift of the valence band was larger than that of Bi^{3+} or Ag^+ (ca. 0.6 eV).

In a previous paper, we examined the photocatalytic activities of $Sn_2Nb_2O_7$, $Sn_2Ta_2O_7$, $SnNb_2O_6$, and $SnTa_2O_6$.[30] Pt-loaded $Sn_2Ta_2O_7$ showed photocatalytic activity for H_2 evolution, whereas $Sn_2Nb_2O_7$ did not, even though they both possess the same pyrochlore structure. Several metal oxide photocatalysts with the pyrochlore structure have been reported.[41,43,44] However, the photocatalytic activity of pyrochlore-structured compounds does not seem high. The activity of Pt-loaded $Sn_2Ta_2O_7$ was actually low. The conduction band level of $Sn_2Nb_2O_7$ is lower than that of $Sn_2Ta_2O_7$. Therefore, the driving force of $Sn_2Nb_2O_7$ for water reduction to form H_2 is not large, resulting in the observation that $Sn_2Nb_2O_7$ hardly shows any activity for H_2 evolution. On the other hand, Pt-loaded $SnNb_2O_6$ showed photocatalytic activity for H_2 evolution, whereas $SnTa_2O_6$ did not. The inactivity of $SnTa_2O_6$ should be due to impurities and defects working as recombination centers between photogenerated electrons and holes, as shown in Figure 1c. Therefore, band structures of tin niobates and tantalates were not relevant to the photocatalytic performances.

3.2. Photocatalytic Properties of $SnNb_2O_6$ under Visible Light Irradiation. Pt-loaded $SnNb_2O_6$ showed photocatalytic activity for H_2 evolution from an aqueous methanol solution under visible light irradiation, as shown in Figure 9. The rate of H_2 evolution was about 9.1 μmol h^{-1} at the initial stage, and the amount of evolved H_2 was 125 μmol for 15 h of reaction time. One might think that Sn^{2+} might be unstable and be oxidized during a photocatalytic reaction. Thermogravimetric analyses were carried out in air to see whether Sn^{2+} in $SnNb_2O_6$ was oxidized to Sn^{4+} by photogenerated holes, as shown in Figure 10. The weight gains of commercial SnO and $SnNb_2O_6$ were 11.8% and 3.9%, respectively. The gains in weight were due to the oxidation of Sn^{2+} to Sn^{4+} by the high-temperature heat

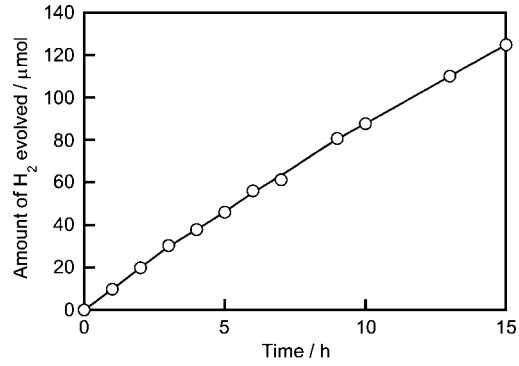

Figure 9. Photocatalytic H_2 evolution from an aqueous methanol solution (150 mL) under visible light irradiation over Pt (0.3 wt %)/$SnNb_2O_6$ powder (0.3 g); light source, 300 W Xe lamp (L42 cutoff filter); cell, top irradiation cell with a Pyrex glass window.

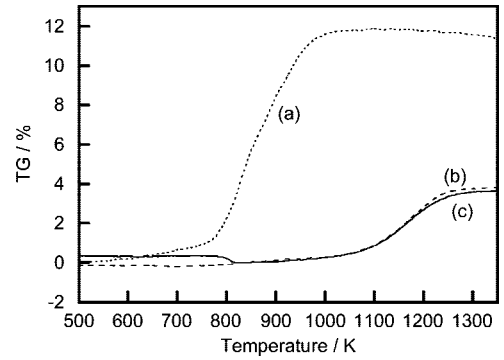

Figure 10. Thermogravimetric analyses of (a) commercial SnO and (b) $SnNb_2O_6$ before and (c) after photocatalytic H_2 evolution.

treatment (673–1273 K) according to eqs 1 and 2, in which the products were confirmed by XRD.

$$Sn^{(II)}O + {}^1\!/_2O_2 \rightarrow Sn^{(IV)}O_2 \quad (1)$$

$$Sn^{(II)}Nb_2O_6 + O_2 \rightarrow Sn^{(IV)}O_2 + Nb_2O_5 + \text{unknown compounds} \quad (2)$$

These weight gains obtained by TGA measurements agreed within 11.9% and 3.9% of the calculated values. It was confirmed that the TG analyses in air were able to be applied to the quantitative analysis for Sn^{2+} in the bulk of metal oxides. Therefore, we investigated the amount of Sn^{2+} in $SnNb_2O_6$ after photocatalytic H_2 evolution by TGA. The difference in the weight gain of $SnNb_2O_6$ comparing before and after H_2 evolution reaction was negligible, as shown in Figure 10b,c. This result indicated that Sn^{2+} in $SnNb_2O_6$ was not oxidized during the photocatalytic reaction.

3.3. Improvement of the $SnNb_2O_6$ Photocatalyst. We examined the preparation conditions and possible modification of the $SnNb_2O_6$ photocatalyst to improve the photocatalytic activity. First, the effects of starting materials and calcination conditions on the photocatalytic activity were investigated. $SnNb_2O_6$ photocatalysts prepared from three different starting materials as Sn sources, commercial SnO, $Sn_3O_2(OH)_2$, and $Sn_3O_2(OH)_2$, calcined at 373 K in air, are denoted by $SnNb_2O_6$(1), $SnNb_2O_6$(2), and $SnNb_2O_6$(3),

(43) Abe, R.; Higashi, M.; Sayama, K.; Abe, Y.; Sugihara, H. *J. Phys. Chem. B* **2006**, *110*, 2219.
(44) Ikeda, S.; Itani, T.; Nango, K.; Matsumura, M. *Catal. Lett.* **2004**, *98*, 229.

Table 1. Photocatalytic Activities of $SnNb_2O_6$ for H_2 or O_2 Evolution from Aqueous Solutions Containing Sacrificial Reagents under Visible Light Irradiation[a]

starting material	calcination condition	photocatalyst	activity/μmol h^{-1} H_2[b]	activity/μmol h^{-1} O_2[c]
$SnO + Nb_2O_5$	1273 K–10 h	$Pt/SnNb_2O_6$(1)	9.1	
		$SnNb_2O_6$(1)		0
		$IrO_2/SnNb_2O_6$(1)		15.3
$Sn_3O_2(OH)_2 + Nb_2O_5$	1323 K–15 h	$Pt/SnNb_2O_6$(2)	14.4	
		$SnNb_2O_6$(2)		5.0
		$IrO_2/SnNb_2O_6$(2)		62.8
calcined $Sn_3O_2(OH)_2 + Nb_2O_5$	1273 K–10 h	$Pt/SnNb_2O_6$(3)	6.3	
		$SnNb_2O_6$(3)		2.9

[a] Catalyst, 0.3 g; light source, 300 W Xe lamp with a cutoff filter (λ > 420 nm). [b] 10 vol % aqueous methanol solution, 150 mL. [c] Aqueous $AgNO_3$ solution: 0.05 mol L^{-1}, 150 mL.

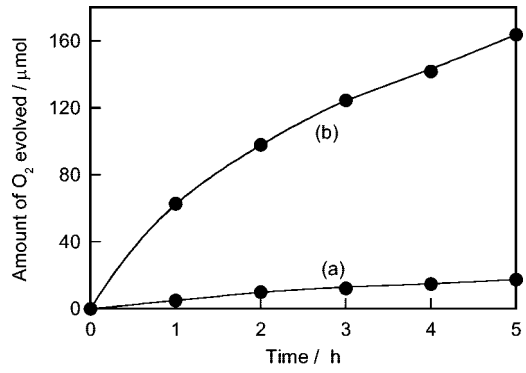

Figure 11. Photocatalytic O_2 evolution from an aqueous $AgNO_3$ solution under visible light irradiation over (a) $SnNb_2O_6$(2) and (b) IrO_2(1 wt %)/$SnNb_2O_6$(2); catalyst, 0.2 g; reactant solution, 0.05 M $AgNO_3$(aq) (150 mL); light source, 300 W Xe lamp (L42 cutoff filter); cell, top irradiation cell with a Pyrex glass window.

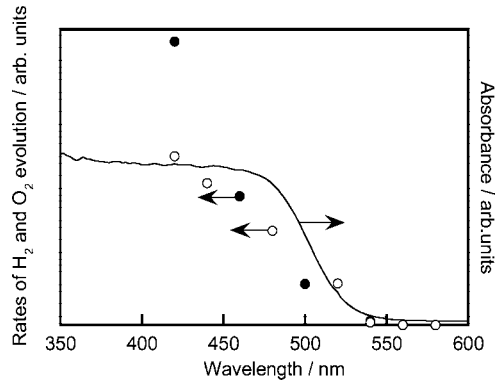

Figure 12. Wavelength dependency for H_2 or O_2 evolution and a diffuse reflectance spectrum of the $SnNb_2O_6$(2) photocatalyst (closed circles, H_2; open circles, O_2). The wavelengths were controlled by cutoff filters.

respectively. Next, modification was carried out by loading a colloidal IrO_2 cocatalyst, which is active for O_2 evolution.[20,45]

Table 1 shows the photocatalytic H_2 or O_2 evolution from water containing sacrificial reagents under visible light irradiation (λ > 420 nm) over $SnNb_2O_6$(1), $SnNb_2O_6$(2), and $SnNb_2O_6$(3). The photocatalytic activities of $SnNb_2O_6$ hardly depended on the calcination conditions. However, the photocatalytic properties of $SnNb_2O_6$ were improved by variation of the Sn source. $Pt/SnNb_2O_6$(2) was the most active for H_2 evolution among the three $Pt/SnNb_2O_6$ photocatalysts. Naked $SnNb_2O_6$(2) and $SnNb_2O_6$(3) showed activity for O_2 evolution from an aqueous silver nitrate solution under visible light irradiation, whereas $SnNb_2O_6$(1) did not. Moreover, the rate of O_2 evolution of $SnNb_2O_6$(2) was faster than that of $SnNb_2O_6$(3). Loading of a colloidal IrO_2 cocatalyst improved the activities for O_2 evolution of $SnNb_2O_6$(1) and $SnNb_2O_6$(2). IrO_2(1 wt %)-loaded $SnNb_2O_6$(2) showed relatively high activity for O_2 evolution, as shown in Figure 11. The turnover number of the amount of O_2 evolved to the amount of loaded IrO_2 was 14 at the 5 h point in the reaction time. The decrease in the O_2 evolution rate with the reaction time was due to the covering of the photocatalyst surface with metallic Ag particles, which decreased the surface reaction sites and shielded the surface from the incident light. The activity of $SnNb_2O_6$ for O_2 evolution should be due to the favorable hydridization of Sn 5s with O 2p at the top of the valence band, as shown in Figure 6. Figure 12 shows the wavelength dependency for the H_2 or O_2 evolution and a diffuse reflectance spectrum of $SnNb_2O_6$(2). The onset of the wavelength dependency of H_2 or O_2 evolution agreed with that of the diffuse reflectance spectrum of $SnNb_2O_6$, indicating that the reaction proceeded photocatalytically with band gap excitation. Although many visible-light-driven photocatalysts for water splitting have been developed, the only valence-band-controlled metal oxide photocatalyst that has shown activity for H_2 evolution under visible light irradiation has been $HPb_2Nb_3O_{10}$.[8] It is noteworthy that the $SnNb_2O_6$ photocatalyst is a novel metal oxide that is active for H_2 or O_2 evolution under visible light irradiation in the presence of sacrificial reagents.

We carried out some characterization to examine the factors responsible for the improvement of the photocatalytic properties of $SnNb_2O_6$(2). The oxidation state and the surface area of the starting materials were investigated. Figure 13 shows the X-ray photoelectron spectra of SnO_2, commercial SnO, and $Sn_3O_2(OH)_2$, the latter both without calcination and with calcination at 373 K in air. The binding energies of Sn $3d_{5/2}$ of SnO_2 and SnO were 486.3 and 485.8 eV, respectively.[46] The obtained spectra were assigned to Sn(II) and Sn(IV) according to the binding energies. Most of the Sn on the surface of the commercial SnO was tetravalent because the surface was easily oxidized in air. In contrast, most of the Sn on the surface of $Sn_3O_2(OH)_2$ was divalent. The Sn on the surface of the $Sn_3O_2(OH)_2$ sample was partly oxidized by calcination at 373 K in air.

(45) Hara, M.; Waraksa, C. C.; Lean, J. T.; Lewis, B. A.; Mallouk, T. E. *J. Phys. Chem. A* **2000**, *104*, 5275.

(46) Pang, G.; Jin, H.; Li, Y.; Wan, Q.; Sun, Y.; Feng, S. *J. Mater. Sci.* **2006**, *41*, 1429.

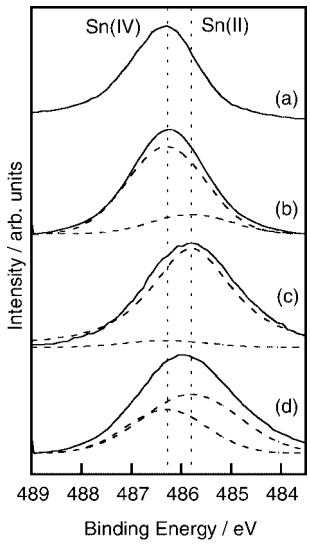

Figure 13. X-ray photoelectron spectra of the Sn $3d_{5/2}$ peak: (a) SnO_2; (b) SnO; (c) $Sn_3O_2(OH)_2$; (d) calcined $Sn_3O_2(OH)_2$ at 373 K in air; dashed line, deconvoluted Sn^{4+} and Sn^{2+}.

The XRD patterns and diffuse reflectance spectra of $SnNb_2O_6(1)$, $SnNb_2O_6(2)$, and $SnNb_2O_6(3)$ exhibit little difference from each other. The morphology of the $SnNb_2O_6$ changed depending on the Sn source. SEM examination revealed that particles of $SnNb_2O_6(1)$ with a size of several micrometers consisted of sintered primary particles (ca. 300 nm), with many grain boundaries, whereas those of $SnNb_2O_6(2)$ had relatively flat surfaces, as shown in Figure 14a,b. The particles of $SnNb_2O_6(3)$ were similar to those of $SnNb_2O_6(1)$, as shown in Figure 14c. Commercial SnO had a smaller surface area (1.0 $m^2\ g^{-1}$) and a larger amount of Sn^{4+} on the surface than $Sn_3O_2(OH)_2$ (30 $m^2\ g^{-1}$). Sn^{4+} on the surface might impede the solid-state reaction. These differences led to the result that the solid-state reaction of $Sn_3O_2(OH)_2$ and Nb_2O_5 to form $SnNb_2O_6$ proceeded more easily than that of commercial SnO and Nb_2O_5. It was concluded that the change in the morphology affected the photocatalytic activity of $SnNb_2O_6$. The low photocatalytic activity of $SnNb_2O_6(1)$ was due to the existence of many grain boundaries, which functioned as recombination sites, while $SnNb_2O_6(2)$, with few grain boundaries, showed good photocatalytic performance, as shown in Table 1.

3.4. Mechanism of Photocatalytic Activity of $SnNb_2O_6$. $SnNb_2O_6(2)$ showed higher photocatalytic activity for H_2 and O_2 evolution from aqueous solutions containing sacrificial reagents than $SnNb_2O_6(1)$. Moreover, a colloidal IrO_2 cocatalyst was indispensable for O_2 evolution on $SnNb_2O_6(1)$, whereas it was not so for $SnNb_2O_6(2)$. These results for the photocatalytic behavior and characterization lead to the reaction scheme shown in Figure 15.

XPS measurements of the SnO starting material suggested that $SnNb_2O_6(1)$ contained a larger amount of Sn^{4+} than $SnNb_2O_6(2)$, although the absolute amount of Sn^{4+} was quite small, judging from the TG measurements, as shown in Figure 10. The Sn^{4+} ion exists at an Nb^{5+} site, judging from the ionic radius and oxidation number. It has also been suggested in the literature that part of the Nb^{5+} ions can be replaced with Sn^{4+} ions in tin niobates.[28] The Sn^{4+} species

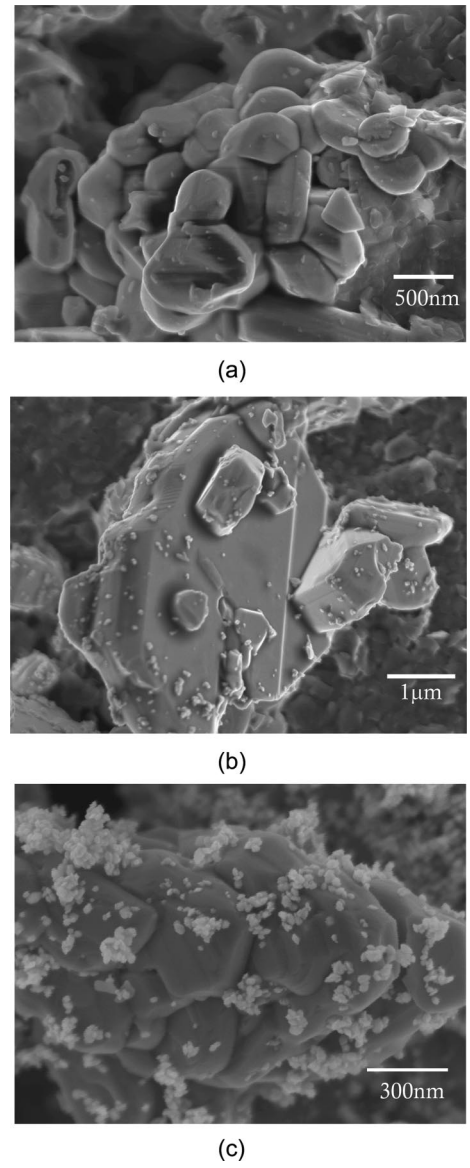

Figure 14. Scanning electron microscope images of (a) $SnNb_2O_6(1)$, (b) $SnNb_2O_6(2)$, and (c) $SnNb_2O_6(3)$.

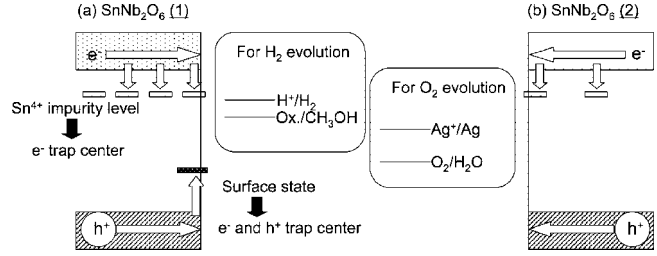

Figure 15. Proposed mechanism of the photocatalytic processes of $SnNb_2O_6(1)$ and $SnNb_2O_6(2)$.

forms an electron trap site below the conduction band, resulting in a decrease in the photocatalytic activity.

The surface of $SnNb_2O_6(2)$ was smooth, while that of $SnNb_2O_6(1)$ was rough due to aggregation of primary particles, as observed by SEM. Surface states would exist on such a rough surface. The surface states trap a part of photogenerated electrons and holes, and decrease their reduction and oxidation potentials, and further work as recombination centers. This also suppresses the direct

reaction of holes in the valence band with methanol and water as reactants.

Thus, the existence of Sn^{4+} and surface states lowered the photocatalytic activity of $SnNb_2O_6$(1) compared with that of $SnNb_2O_6$(2) and made O_2 evolution accompanied by four-electron oxidation unfavorable. Colloidal IrO_2 cocatalyst assists the O_2 evolution by the reaction of water with holes in the valence band and surface states, as shown in Table 1 and Figure 11.

4. Conclusions

It was revealed from diffuse reflectance spectra and PW-DFT calculations that the band gaps of SnM_2O_6 and $Sn_2M_2O_7$ (M = Nb and Ta) became narrower than those for typical niobates and tantalates due to the valence bands consisting of Sn 5s orbitals. In particular, $SnNb_2O_6$ was found to be an active photocatalyst that evolved H_2 or O_2 from aqueous solutions containing sacrificial reagents under visible light irradiation ($\lambda > 420$ nm). The photocatalytic activity for O_2 evolution was remarkably increased when an IrO_2 cocatalyst was loaded. The photocatalytic activity of $SnNb_2O_6$ was improved by using $Sn_3O_2(OH)_2$ as a starting material, which contained a negligible amount of Sn^{4+} impurity. The results of these experiments, together with the characterization, suggest that the suppression of the formation of Sn^{4+} as an impurity and of grain boundaries should improve the photocatalytic performance. Thus, the control of valence bands by Sn^{2+} is one of the guides to develop a visible-light-driven photocatalyst for water splitting as well as that by Ag^+ and Bi^{3+}.

Acknowledgment. This work was supported by the Core Research for Evolutional Science and Technology (CREST) program of the Japan Science and Technology Agency (JST), a Grant-in-Aid (No. 14050090) for the Priority Area Research (No.417) from the Ministry of Education, Culture, Sports, Science and Technology (MEXT) of Japan, and the Nissan Science Foundation.

Supporting Information Available: Additional tables of crystal parameters for the plane-wave-based density functional calculations. This material is available free of charge via the Internet at http://pubs.acs.org.

CM071588C